



Published in final edited form as:

Proc IEEE Int Symp Bioinformatics Bioeng. 2020 October ; 2020: 472–480. doi:10.1109/bibe50027.2020.00082.

Fusion Learning on Multiple-Tag RFID Measurements for Respiratory Rate Monitoring

Stephen Hansen, Daniel Schwartz, Jesse Stover, Md Abu Saleh Tajin, William M. Mongan, Kapil R. Dandekar

Department of Electrical and Computer Engineering, Drexel University, Philadelphia, PA USA

Abstract

Future advances in the medical Internet of Things (IoT) will require sensors that are unobtrusive and passively powered. With the use of wireless, wearable, and passive knitted smart garment sensors, we monitor infant respiratory activity. We improve the utility of multi-tag Radio Frequency Identification (RFID) measurements via fusion learning across various features from multiple tags to determine the magnitude and temporal information of the artifacts. In this paper, we develop an algorithm that classifies and separates respiratory activity via a Regime Hidden Markov Model compounded with higher-order features of Minkowski and Mahalanobis distances. Our algorithm improves respiratory rate detection by increasing the Signal to Noise Ratio (SNR) on average from 17.12 dB to 34.74 dB. The effectiveness of our algorithm in increasing SNR shows that higher-order features can improve signal strength detection in RFID systems. Our algorithm can be extended to include more feature sources and can be used in a variety of machine learning algorithms for respiratory data classification, and other applications. Further work on the algorithm will include accurate parameterization of the algorithm's window size.

Keywords

Sensor fusion; Machine learning algorithms; Signal denoising

I. Introduction

The applications of Radio-Frequency Identification (RFID) technology have grown beyond its original applications of inventory, tolling, or keyless entry into vehicles and buildings [1]. As RFID has become ubiquitous in many of today's industries, its popularity has led to many advanced uses such as tracking of human motion, gesture recognition, and epidermal implants in healthcare [2]. However, there are limitations which encourage research into refining the use of RFID beyond its original use. Foremost and subject to public scrutiny are the challenges of privacy and overuse of RFID technology [3]. More relevant to our paper are the physical limitations of read range, path loss, and changes in antenna characteristics upon contact with different surfaces, such as the human body [4].

The main focus of this paper is infant respiratory monitoring using RFID technology and knitted antennas as a strain-gauge sensor. Fig. 1 shows our device called the “Bellyband” worn by a medical mannequin simulator (Laerdal SimBaby) used to simulate medical scenarios. The tensile characteristics of knitted antennas is what facilitates the quantification of strain on the antenna. This is possible because the strength of a signal transmitted from an RFID tag changes as: i.) the surface area of the antenna changes, ii.) the resonant frequency of the antenna changes, and iii.) coupling between the antenna and the inductively-coupled RFID chip varies. These electromagnetic effects decrease the Received Signal Strength Indicator (RSSI) values received from the RFID tag [5]. Therefore, tracking the change in RSSI values allows us to track electromagnetic changes to the antenna and infer changes in breathing state. From there, we can compare our predictions to ground truth data to ascertain the accuracy of our system.

The use of wearable knitted tensile antennas for monitoring of strain-gauge based activities poses its own problems through multipath fading and electromagnetic coupling. The desired RFID signal and multipath reflections from other objects in the room will interfere with each other, resulting in constructive and destructive interference and temporal lag (*i.e.*, multipath fading). Because a signal propagated through RFID can be very weak, even small-scale fading has been shown to cause significant loss in signal resolution [6]. In this study, we use a second stationary, non-stretched reference antenna to model temporal artifacts and the multipath fading profile of the “main” Bellyband antenna worn about the abdomen. With this profile, we create a time-series representing the similarity of the two signals using the Mahalanobis distance measure, from which we can infer respiratory activity. This algorithm can remove non-respiratory artifacts from the Bellyband’s RFID signal, regardless of it coming from fading or any other source.

We first use a Regime Hidden Markov Model to cluster respirations via predicting data from the main antenna as belonging to one of two distributions, one that contains data where the Bellyband is stretched, and another where it is fixed relaxed. This is repeated with the reference antenna’s signal, clustering its data points into two distributions containing coupled and non-coupled data. Using a Markov Chain Monte Carlo (MCMC) we then perform a Metropolis random-walk [7] to further refine the predicted prior distributions.

A Z-test is used in real-time to separate data points from each antenna into one of the distributions predicted by the MCMC. In order to compare the signals received from each antenna with respect to time, they are sampled by a sliding window. Because of the non-tethered nature of a passive wearable textile-based sensor, this also has the potential to detect and remove mechanical artifacts like a person ambulatory during monitoring.

II. Related Work

A. Respiration Monitoring

The invasive nature of respiratory monitoring methods can be limiting in specific medical contexts where ambulatory patients cannot be tethered to electrodes or a CO₂ monitoring apparatus. The use of masks, belts, or nose pieces can also be disturbing to the subject resulting in deviation from the normal tidal volume or respiratory rate of automatic breathing

[8], [9]. For example, the use of belts for the detection of sleep apnea has similar obtrusive effects due to restriction of a patient's breathing or loosening of the belt if there is movement during sleep [10]. The use of a wearable tensile antenna rectifies many of these issues by utilizing RFID backscatter signal strength and the measurement of strain-gauge movements to detect respiratory artifacts. This provides comfort and allows a patient to be ambulatory.

B. RFID for Biomedical Sensing

Many studies have proposed novel approaches to the use of RFID technology. To alleviate discomfort of patients and increase reliability of sleep apnea diagnosis, an experimental contactless ultra-wide band system is being developed [10]. We have previously applied RFID technology to detection of sleep apnea [11], uterine activity during labor [12], monitoring of heart rate [13], and management of Deep Vein Thrombosis (DVT) [14]. We have previously proposed a sensor-fusion framework for the reclassification of data misclassified by a single main antenna for the detection of sleep apnea [15]. However, in this study we aim to expand upon a data fusion setup to denoise a signal and facilitate the prediction of respiratory artifacts with greater accuracy. With this sensor-fusion framework, we can also identify and remove data transmitted from the reference antenna when it is coupled to the main antenna. These RFID applications overcome limitations due to the physical properties of RF transmission from passive RFID tags. Some studies aim to increase the accuracy of interrogating backscatter signals [16], [17]. One study analyzes other RFID signal features such as channel state information, which could be used in our future work [18].

C. Deep Learning

Deep Learning is a popular mechanism used to denoise RF signals via residual learning. Deep Learning methods estimate the denoised signal by adding a white Gaussian noise channel and Rayleigh fading channel effects [19]. Another use of Deep Learning is convolutional autoencoders, which are trained to find a deep embedding for data inputs by repeatedly convolving the data with a random process. Specifically, one study [20] removed noise contamination of signals via unsupervised convolutional autoencoders. These autoencoders significantly improved signal-to-noise ratio without any prior knowledge of the model.

Other research [21] has leveraged channel state information and Principal Component Analysis to denoise extracted features. These researchers used a mean filter to remove most noise, but it also removed significant details relating to accurate information. A low-pass Butterworth filter also removed noise, but had slow fall off. There has also been some research in leveraging radio frequency channel fluctuation for activity recognition. The velocity of an entity was estimated by analyzing the RSSI pattern of the moving node and exploited the fluctuation in the time evolution of the strength received of the signal [22]. Another approach for denoising RF data applies a non-local approach that exploits redundancy in the signal and uses a weighted average of the most similar components [23]. The proposed approach, Coherent Denoising for Elastography (CODE), had superior results to its competitors (i) GLocal Ultrasound Elastography (GLUE) [24], and; (ii) Dynamic Programming Analytic Minimization elastography (DPAM) [25].

III. Approach

A. Overview

Each stage of our proposed algorithm is captured in Fig. 2. These stages include: i.) input of two RF channels, ii.) state classification and separation, iii.) sliding window processing, iv.) high-order feature extraction, and v.) sensor fusion with Mahalanobis distance. Lastly, the SNR and accuracy of rate estimation of our input and output signals are measured and compared to quantify the increase in signal quality.

At the input level, two RFID features are read from our sensor framework for each tag interrogation: RSSI values and the Doppler shift. We compute the tag velocity by observing the change in Doppler shift with respect to the interrogation frequency and interrogator antenna gain [17]. The RSSI values represent the change in electromagnetic properties of the main antenna and velocity represents non-respiratory movement, which can be used to discern and remove incidental movement of the wearer.

For each antenna, a Regime Hidden Markov Model predicts two hidden states [26]. A Metropolis random walk is performed using a Markov Chain Monte Carlo (MCMC) to refine the predicted distributions describing these states [7]. With a Z-test, RSSI and velocity data from each tag are then separated. Each data point is grouped into one of the distributions predicted by the MCMC, which describe stretching or fixed relaxed states for the main antenna and coupled or non-coupled states for the reference antenna. With this application, the Mahalanobis distance [27] is computed between the main antenna and reference antenna distributions within each sliding window and interpolated over the entire data set.

RSSI values are discrete in nature, and with noise effects included, respiration would lead to only small changes in RSSI amplitude. Because of this small dynamic range, signals can have very low resolution, resulting in a high covariance between the two distributions being measured. The Mahalanobis distance requires the inverse (2×2) covariance matrix of these two distributions; if the covariance is too high, the distribution matrix will be singular and an inverse matrix cannot be computed. To mitigate a singular matrix, a windowed Minkowski distance [28] is added as a higher-order feature as outlined in Section III-D to decrease covariance. However, in case a singular matrix is still encountered, the identity matrix is used instead of its inverse.

Calculating a windowed Mahalanobis distance with the three signal features illustrated in Fig. 4 and interpolating over the data set outputs a final “denoised” signal. We quantify the increase in breathing signal quality by calculating and comparing the Signal to Noise Ratio of the raw input and final transformed signals.

B. State Classification using Switching HMM and MCMC

Since the two RFID tags may be coupled due to close proximity, a Switching Hidden Markov Model (Switching HMM) and Markov Chain Monte Carlo (MCMC) are leveraged to predict two distributions representing an estimated grouping of the data points from the main antenna corresponding to respiratory activity and data points corresponding to non-

respiratory pauses between breaths (“noise”). The distribution with a lower mean, implying the main antenna is stretched and out of phase with the interrogator, represents stretching (“inhaled”) data. The distribution with a greater mean, implying the main antenna is resting and in phase, represents fixed-relaxed (“exhaled”) data. A Z-test is then used to classify each point in time as belonging to one distribution or another. This separation is illustrated in Fig. 3. This classification is repeated with the reference antenna, classifying data into coupled and non-coupled distributions. Data points belonging to the reference antenna’s coupled state are then ignored to mitigate coupling between the main and reference tags during wearer movements.

The Switching HMM uses a semi-supervised approach, initialized with 30 seconds of data assumed to contain respiratory data. The respiratory rate is not provided to the Switching HMM and instead it searches for neighboring clusters of data belonging to either of its hidden states. Following classification, we predict which distributions represent the main antenna’s stretching or fixed relaxed states, and the reference antenna’s coupled or non-coupled states. The data points of each antenna are classified as belonging to one of these hidden states by estimating the means and standard deviations of these “hidden” distributions [26]. Once the distributions are estimated, gradient descent and maximum likelihood estimation are combined to identify probabilities of a data point being assigned to a given class. Gradient descent is then able to find a point of convergence within the Switching HMM. The distributions estimated by the Switching HMM are then used by the MCMC to perform a “random walk” to converge to an accurate representation of the distributions that correspond to each of the antenna’s states without needing to train on a large data set.

C. Sliding Window Processing

The prediction process is iterated over both the main and reference antennas. The features of each predicted distribution are then handed to a Z-test which assigns each point in time to one antenna or the other, for each respective signal. The signal from the main antenna now only contains stretching state data, and that of the reference antenna only contains non-coupled state data; we now consider only these two signal distributions. Timestamps are preserved to maintain temporal alignment of these two signals. Once each point is attributed to one distribution or another, we apply a sliding window of size n (one quarter of the estimated respiratory rate) and a stride $k = \frac{n}{4}$ to sample data from the two distributions of interest.

D. High-order Feature Extraction with Minkowski Distance

After separating RSSI and Doppler values into two distributions, the windowed Mahalanobis distance measures between the two distributions fails because of a high covariance between the main and reference antennas when a low-resolution signal is present. The Minkowski distance (Equation 1) is a metric in a normed vector space that can be considered a generalization of both the Euclidean (order 2) and Manhattan distance (order 1) [28]. We set the order h to 20 for the Minkowski distance to increase its concentration leveraging Chebyshev’s inequality [28]. The Minkowski distance apart from the supremum distance

(Chebyshev distance) can also be represented as a multiple of the power mean of the component-wise differences between the two entities.

$$d(i, j) = \sqrt[h]{|x_{i1} - x_{j1}|^h + |x_{i2} - x_{j2}|^h + \dots + |x_{ip} - x_{jp}|^h} \quad (1)$$

Because there is only one value per window instead of a time series, these values aren't immediately appended to their respective windows. Instead they are placed in the exact point of time where the window begins with respect to the whole data set. A linear interpolation of these discrete points seen in Fig. 4 is then calculated. The same windowed sampling algorithm as before is applied to these time series and then combined with the existing windows.

E. Mahalanobis Distance

Once we have increased the dimensionality, these windowed distributions no longer have high covariance and can be used in the Mahalanobis distance measure. This measure outputs an $N \times N$ matrix where N is the length of the windowed distributions being compared. To output a single distance measure we take the Euclidean distance of the diagonal of this output matrix, which then represents the number of standard deviations the two distributions are from each other. Low deviation indicates similarity of the main and reference signals.

We use the Mahalanobis distance (Equation 2) to compute the distance between an observation in the main signal and the concurrent observation in the reference signal. Note that \vec{x} is an n -dimensional observation, \vec{r}_μ is the mean of the n -dimensional reference distribution observations, and S is an $n \times n$ covariance matrix of the main and reference distributions, where n is the dimensionality of each distribution.

$$D_M(\vec{x}) = \sqrt{(\vec{x} - \vec{r}_\mu)S^{-1}(\vec{x} - \vec{r}_\mu)^T} \quad (2)$$

For each window, we compute the covariance matrix S of the reference and main distributions. We calculate the Mahalanobis distance D_M for the distribution x in the main window against the distribution r_μ in the reference window and the covariance matrix S . Subtracting the distributions and multiplying by the inverse covariance matrix yields the number of standard deviations squared between every observation in both distributions, an $N \times N$ matrix. The square root of the diagonal of this $N \times N$ matrix yields the final Mahalanobis distance between the two windowed distributions.

IV. Experimental Setup

A. Channel Emulation Hardware

We construct a channel emulation board (Fig. 5) that allows us to emulate wireless channels in a wired and controlled setup without the need of reader and tag/sensor antennas [29]. The emulation board is a $30 \text{ mm} \times 21 \text{ mm} \times 1.5 \text{ mm}$ FR4-based PCB (Printed Circuit Board) structure. A Monza R6 RFID chip is soldered at one end of the board, and an SMA (Sub-Miniature Version A) connector is soldered on the other end. The RFID chip is a balanced

circuit. In other words, the two pads of the chip are electrically 180° apart. On the other hand, the SMA is a unbalanced connector with a ground conductor. A 1:1 balun (balanced to unbalanced converter) is placed between the chip and the connector that converts the balanced ports of the chip to unbalanced ports, without changing the chip impedance.

We use the Echo Ridge DYnamic Spectrum Environment Emulator (DYSE) [30] to provide time-varying channel characteristics. Fig. 6 shows the hardware setup for dual-channel emulation. An Impinj Speedway R420 RFID reader is connected to a 2:1 power divider. The two output ports of the divider are isolated from each other. As a result, we create two independent channels; each channel consists of a couple of RF circulators, a DYSE channel, an RF attenuator, and one emulation board. Each circulator has three RF ports that allow RF signals in a certain circular fashion (1 to 2, 2 to 3, and 3 to 1). This behavior of RF circulators allows us to separate the forward and reverse channels. Since the Monza R6 chip is passive, it is dependent on the power from the reader for running its circuitry and communication. The RFID chip on the emulation board accepts a fixed amount of power coming from the reader via the forward path and reflects the rest by modifying the chip impedance. We observe that emulating the reverse path is equivalent to the simultaneous emulation of both forward and reverse paths. Moreover, the DYSE has a maximum power tolerance around -15 dBm, which is very close to the wake-up threshold of the RFID chip (≈ 16 dBm). We place an attenuator on the forward path and the DYSE on the reverse. The return signal reflected from the emulation board passes through a DYSE channel that emulates the gain variation of the wearable antenna. Upon passing through the separate DYSE channels, the return signals from both RFID chips are combined and delivered to the reader.

B. Data Collection

Our DYnamic Spectrum Environment emulator uses one emulation board fit with a Monza R6 RFID tag for each channel emulated. The fluctuating attenuation of signal strength in one channel represents the RSSI activity of a stretching Bellyband main antenna in clean experimental conditions. The fixed attenuation in the other channel represents the “noisy” RSSI activity of a non-coupled reference antenna under normal conditions. Because the emulation doesn’t incorporate any multipath or temporal delay features, we augment the emulated output signal with Rayleigh fading. The Rayleigh fading model exhibits the effect of interfering signals coming from all directions surrounding the interrogator.

C. Rayleigh Fading Model

With the DYSE, one reference and two main signals are produced at rates of 0, 15, and 30 breaths/minute, respectively. To create a collection of viable data sets for experimentation, these signals are iteratively transformed with random sampling from a Rayleigh fading model which emulates multi-path fading and temporal lag.

A two-dimensional epsilon factor ϵ is randomly sampled from a Rayleigh distribution $p(x, y)$ parameterized by the data set’s original features and added to each data point. Here each data point (x, y) corresponds to a pair of RSSI and velocity values recorded at any given point in time. This factor is normalized according to the mean of the Rayleigh distribution μ .

A noise factor C is used to scale the introduced fading to emulate environments which induce different levels of interference $\left(\epsilon = \frac{p(x,y) - \mu}{\mu} \cdot C\right)$. According to its value, ϵ may also be displaced in time by a factor equal to the floor of its magnitude. The resulting data point is then rounded to the nearest discrete RSSI value. This approach can be considered a “worst-case scenario” that would result from the signal being received by the interrogator from all directions.

D. Quantification

Once we compute a single-channel transformed signal, we compare it to the raw input signal from the main antenna using an SNR calculation. For the sake of experiment, we isolate data with a known ground-truth respiratory rate. For each signal, a Fast Fourier Transform is calculated and the spectral centroid ω nearest our desired frequency is calculated and isolated. The frequencies f_{bin} and magnitudes $P_{\text{bin,dB}}$ of the bins immediately neighboring the desired frequency bin $k = -1, 0, 1$ are used, as shown in Equation 3.

$$w = \frac{\sum_{k=-1}^1 f_{\text{bin}} P_{\text{bin,dB}}}{\sum_{k=-1}^1 P_{\text{bin,dB}}} \quad (3)$$

The magnitude of this frequency centroid is $P_{\text{signal,dB}}$ and the sum of the magnitudes of all other bins is $P_{\text{noise,dB}}$. To normalize the numerator, the magnitude of the desired frequency bin is multiplied by the total number of frequency bins less the three bins ($k = -1, 0, 1$) used to locate the centroid ($N - 3$), as shown in Equation 4.

$$\text{SNR}_{\text{db}} = P_{\text{Signal,dB}} - \frac{P_{\text{noise,dB}}}{N - 3} \quad (4)$$

The increase in SNR, SNR , from the raw signal to transformed signal and the final $P_{\text{signal,dB}}$ are used to quantify the increase in signal quality from using our denoising algorithm. An increase in SNR without loss of $P_{\text{signal,dB}}$ would signify filtering of unwanted high-frequency components without the loss of respiratory information. A greater $P_{\text{signal,dB}}$ would in turn suggest the transformed signal more accurately represents the actual respiratory signal.

V. Results and Discussion

With our DYSE wireless channel emulation system we emulated two attenuating signals, one corresponding to 15 breaths per minute, and the other 30 breaths per minute, each for 60 seconds. A 60 second, 0 breaths per minute signal is emulated and added to each data set as the reference antenna’s signal. After being passed through our Rayleigh fading model, the first 30 seconds of data are used for classification and training by the switching Markov model and MCMC simulation.

Fig. 8a represents the remaining 30 seconds of data that is used as input to our Mahalanobis algorithm from a signal with a breathing rate of 30 breaths per minute, a sampling rate of 40

Hz , and a noise scale $C = 3$. The “inhaled” stretching state corresponds to regions with lower RSSI values. When the wearer exhales, the RSSI will then increase as the antenna compresses and returns to its “exhaled” fixed-relaxed state. The high-frequency components of the signal resulting from fading decrease SNR and are what interfere with accurate classification and prediction of respiratory artifacts such as rate, breathing state, or cessation of breathing.

Fig. 8b represents the transformed signal after being passed through our algorithm. This signal represents the number of standard deviations each window of attenuating data points is from the concurrent window of stationary data points across the N dimensions used for analysis. In this case, the standard deviations are measured with respect to the decibels of the original input signals. So, the output signal itself represents the similarity of the attenuating and stationary signals with respect to time, interpreted in decibels.

Comparing Fig. 8b to Fig. 8a shows a large decrease in the high-frequency components that decrease SNR and inhibit breathing state classification. The spectral centroid of the input signal shown in Fig. 8a has frequency of $0.484 Hz$ and a magnitude of $-13.29 dB$, and that the output has a frequency of $0.517 Hz$ and a magnitude of $-6.84 dB$. With this increased magnitude and decreased high-frequency components, we can yield a closer estimate of the desired respiratory rate, with a change in SNR of $20.68 dB$.

Figures 8c and 8d represent the two signals' Fast Fourier Transforms (FFTs), respectively. The spectral centroid used in our SNR calculation of each is the point (x, y) highlighted in red, where x is its frequency and y its magnitude. A logarithmic horizontal axis is used in order to analyze the frequency bins neighboring the spectral centroid, which only make up a very small portion of the entire spectrum. A large decrease in the high-frequency components of the signal can be observed between the raw and transformed signal FFTs for frequencies greater than $1 Hz$. In this regard, the Mahalanobis distance transformation behaves as a high-pass filter, attenuating frequency components above the spectral centroid and increasing the SNR of the breathing signal.

In figures 8a through 8d, a sliding window length $n = 1$ second and window slide $k = 0.25$ seconds were used. These values were chosen according to results gained by manual testing. Because of the discrete nature of frequency bins, decoupling of the relationship between breathing rate and sliding window parameters results in spectral leakage. Improper parameterization then can lead to inaccurate predictions of the spectral centroid, a decrease in SNR, and potentially a loss of respiratory information. Therefore, we use the current estimate of the respiratory rate to assign our algorithm parameters over time. Table I shows results averaged across 20 trials of each scenario. The raw signal is that read directly from the main antenna, and the transformed is that output by our algorithm. SNR values and the magnitude of the spectral centroids are calculated for each trial then averaged across each scenario.

For each triplet of scenarios with unique values of C , SNR and $P_{\text{signal,dB}}$ both decrease as C is increased. However, the change in SNR tends to increase because more unwanted high-frequency components are being filtered out of the signal. This high-pass filtering effect of

the Mahalanobis distance algorithm can also be seen in Figures 8b and 8d. Overall, as fading becomes a greater factor in the destruction of the input signal, our Mahalanobis algorithm becomes more effective, which can be seen as C is increased.

VI. Conclusion and Future Work

In this paper, we proposed an algorithm that fuses two RFID signals to remove multipath fading and temporal artifacts. One signal is received from a main antenna that transmits respiratory strain-gauge data. The other is received from a stationary reference antenna that represents the main antenna's fixed-relaxed state. A Regime Hidden Markov Model, Markov Chain Monte Carlo, and Z-test are used to separate each signal into two hidden states. The states identified as the main antenna's stretching state and reference antenna's non-coupled state are then used for sensor fusion.

Sliding window sampling is applied to the separated data, and a Minkowski distance is then calculated between each window's RSSI and velocity values. A Mahalanobis distance is then used to measure the number of standard deviations between concurrent windows. These windowed distances are then interpolated over the entire dataset to output a final denoised strain-gauge signal from the fusion of our reference and main antennas. A comparison of the raw and transformed signals' SNRs are then leveraged to quantify the improvement in signal quality. The average SNR of all faded signals before transformation was 17.12 dB. The average of all transformed signals was 34.74 dB (an average improvement of 17.62 dB).

This algorithm monitors physical changes in RFID signals. Combining it with systems monitoring biological signals can lay the foundation for ML-based respiratory artifact prediction. This can include adaptive filtering dependent upon the breathing rate, correlation of heart and breathing rates, and the detection of other respiratory artifacts. Accurate respiratory classification by the Bellyband can be applied to dynamic scenarios such as ventilators producing oxygen in phase with breathing or active life-support systems. The SNR algorithm designed for this study can be also used to quantify the increase in signal quality by other transformation algorithms.

Acknowledgement

Our research results are based upon work supported by the National Science Foundation Division of Computer and Network Systems under award number CNS-1816387 and award number CNS-1711773. Any opinions, findings, and conclusions or recommendations expressed in this material are those of the author(s) and do not necessarily reflect the views of the National Science Foundation. Research reported in this publication was supported by the National Institutes of Health under award number R01 EB029364-01. The content is solely the responsibility of the authors and does not necessarily represent the official views of the National Institutes of Health.

References

- [1]. Landt J, "The History of RFID," IEEE Potentials, vol. 24, pp. 8–11, 2005. [Online]. Available: 10.1109/MP.2005.1549751
- [2]. Amendola S, Lodato R, Manzari S, Occhiuzzi C, and Marrocco G, "RFID Technology for IoT-based Personal Healthcare in Smart Spaces," IEEE Internet of Things Journal, vol. 1, pp. 144–152, 2014. [Online]. Available: 10.1109/JIOT.2014.2313981

- [3]. Ohkubo M, Suzuki K, and Kinoshita S, "RFID Privacy Issues and Technical Challenges," *Communications of the ACM*, vol. 48, pp. 66–71, 2005. [Online]. Available: 10.1145/1081992.1082022
- [4]. Nikitin PV and Rao KVS, "Performance Limitations of Passive UHF RFID Systems," *IEEE Antennas and Propagation Society, AP-S International Symposium (Digest)*, vol. 2006, pp. 1011–1014, 2006. [Online]. Available: 10.1109/APS.2006.1710704
- [5]. Patron D, Mongan W, Kurzweg TP, Fontecchio A, Dion G, Anday EK, and Dandekar KR, "On the Use of Knitted Antennas and Inductively Coupled RFID Tags for Wearable Applications," *IEEE Transactions on Biomedical Circuits and Systems*, vol. 10, p. 6, 2016. [Online]. Available: 10.1109/TBCAS.2016.2518871.
- [6]. Griffin JD and Durgin GD, "Multipath Fading Measurements for Multi-Antenna Backscatter RFID at 5.8 GHz," in *2009 IEEE International Conference on RFID*, pp. 322–329 [Online]. Available, 2009.
- [7]. Metropolis N and Ulam S, "The Monte Carlo Method," *Journal of the American Statistical Association*, vol. 44, no. 247, pp. 335–341, 1949. [Online]. Available: <http://www.jstor.org/stable/2280232> [PubMed: 18139350]
- [8]. Askanazi J, Silverberg PA, Foster RJ, Hyman AI, Milic-Emili J, and Kinney JM, "Effects of Respiratory Apparatus on Breathing Pattern," *Journal of Applied Physiology Respiratory Environmental and Exercise Physiology*, vol. 48, pp. 577–580, 1980. [Online]. Available: 10.1152/jap.1980.48.4.577
- [9]. Gilbert R, Auchincloss JH, Brodsky J, and Boden W, "Changes in Tidal Volume, Frequency, and Ventilation Induced by their Measurement," *Journal of Applied Physiology*, vol. 33, pp. 252–254, 1972. [Online]. Available: 10.1152/jap.1972.33.2.252 [PubMed: 5054434]
- [10]. Nijssure Y, Tay WP, Gunawan E, Wen F, Yang Z, G. Z. YL, and Chua AP, "An Impulse Radio Ultrawideband System for Contactless Noninvasive Respiratory Monitoring," *IEEE Transactions on Biomedical Engineering*, vol. 60, pp. 1509–1517, 2013. [Online]. Available: 10.1109/TBME.2012.2237401 [PubMed: 23314764]
- [11]. Mongan WM, Rasheed I, Ved K, Levitt A, Anday E, Dandekar K, Dion G, Kurzweg T, and Fontecchio A, "Real-time Detection of Apnea via Signal Processing of Time-series Properties of RFID-based Smart Garments," *2016 IEEE Signal Processing in Medicine and Biology Symposium, (SPMB)*, vol. 1, 2017. [Online]. Available: 10.1109/SPMB.2016.7846871
- [12]. Mongan W, Anday E, Dion G, Fontecchio A, Joyce K, Kurzweg T, Liu Y, Montgomery O, Rasheed I, Sahin C, Vora S, and Dandekar K, "A Multi-Disciplinary Framework for Continuous Biomedical Monitoring Using Low-Power Passive RFID-Based Wireless Wearable Sensors," in *2016 IEEE International Conference on Smart Computing. IEEE*, 2016, pp. 1–6.
- [13]. Vora SA, Mongan WM, Anday EK, Dandekar KR, Dion G, Fontecchio AK, and Kurzweg TP, "On Implementing an Unconventional Infant Vital Signs Monitor with Passive RFID Tags," in *2017 IEEE International Conference on RFID. RFID 2017*: [Online]. Available, 2017, pp. 47–53.
- [14]. Gentry A, Mongan W, Lee B, Montgomery O, and Dandekar KR, "Activity Segmentation Using Wearable Sensors for DVT/PE Risk Detection," *IEEE 43rd Annual Computer Software and Applications Conference (COMPSAC)*, vol. 477, 2019. [Online]. Available: 10.1109/COMPSAC.2019.10252
- [15]. Acharya S, Mongan WM, Rasheed I, Liu Y, Anday E, Dion G, Fontecchio A, Kurzweg T, and Dandekar KR, "Ensemble Learning Approach via Kalman Filtering for a Passive Wearable Respiratory Monitor," *IEEE Journal of Biomedical and Health Informatics*, vol. 23, pp. 1022–1031, 2019. [Online]. Available: 10.1109/JBHI.2018.2857924 [PubMed: 30040664]
- [16]. Alfian G, Syafrudin M, Yoon B, and Rhee J, "False Positive RFID Detection Using Classification Models," *Applied Sciences*, vol. 9, p. 6, 2019. [Online]. Available: 10.3390/app9061154
- [17]. Han J, Ding H, Qian C, Ma D, Xi W, Wang Z, Jiang Z, and Shangguan L, "CBID: A Customer Behavior Identification System Using Passive Tags," *Proceedings - International Conference on Network Protocols, ICNP*, pp. 47–58, 2014.
- [18]. Yang Z, Zhou Z, and Liu Y, "From RSSI to CSI: Indoor Localization via Channel Response," *ACM Computer Survey*, vol. 46, p. 2, 12 2013. [Online]. Available: 10.1145/2543581.2543597

- [19]. Wang Y, Tu L, Guo J, and Wang Z, "Residual Learning Based RF Signal Denoising," pp. 15–18, 2018.
- [20]. Rothenhaus J, Usn CO, and Keeney C, Radio Model-free Noise Reduction of Radio Transmissions with Convolutional Autoencoders, 2017.
- [21]. Chun-xiang WU, Han SU, and Kai YU, A Wireless Signal Denoising Model for Human Activity Recognition. DEStech Transactions on Computer Science and Engineering, 2016.
- [22]. Sigg S, Shi S, Büsching F, Ji Y, and Wolf LC, Leveraging RF-channel Fluctuation for Activity Recognition: Active and Passive Systems, Continuous and RSSI-based Signal Features. In MoMM, 2013.
- [23]. Khavari P, Asif A, Boily M, and Rivaz H, "Nonlocal Coherent Denoising of RF Data for Ultrasound Elastography," Journal of Healthcare Engineering, vol. 2018, p. 06, 2018.
- [24]. Hall T, Barbone P, Oberai A, Jiang J, Dord J-F, Goenezen S, and Fisher T, "Recent Results in Nonlinear Strain and Modulus Imaging," Current Medical Imaging Reviews, vol. 7, p. 11, 2011.
- [25]. Ophir J, Alam K, Garra B, Kallel F, Konofagou E, Krouskop T, and Varghese T, "Elastography: Ultrasonic Estimation and Imaging of the Elastic Properties of Tissues," Proceedings of the Institution of Mechanical Engineers. Part H, Journal of Engineering in Medicine, vol. 213, p. 02, 1999.
- [26]. Mongan WM, "Predictive Analytics on Real-Time Biofeed-back for Actionable Classification of Activity State," PhD Dissertation, Drexel University, 2018. [Online]. Available: <http://www.billmongan.com/files/mongan-dissertation.pdf>
- [27]. Maesschalck RD, Jouan-Rimbaud D, and Massart DL, "The Mahalanobis Distance," Chemometrics and Intelligent Laboratory Systems, vol. 50, no. 1, pp. 1 – 18, 2000. [Online]. Available: <http://www.sciencedirect.com/science/article/pii/S0169743999000477>
- [28]. Singh A, Yadav A, and Rana A, "K-means with Three Different Distance Metrics," International Journal of Computer Applications, vol. 67, no. 10, 2013.
- [29]. Tajin MAS, Jacovic M, Mongan W, and Dandekar KR, "Channel Emulation for the Characterization of Wearable RFID Systems," IEEE Wireless and Microwave Technology Conference, WAMICON 2020, unpublished.
- [30]. Ridge Echo. DYSE - DYnamic Spectrum Environment Emulator. [Online]. Available: <https://www.echoridgenet.com/products/dyse>



Figure 1:

The Bellyband can be seen here worn around the Laerdal SimBaby's waist. There are no wired connections or additional nodes required for its function. As the torso expands upon inhalation, the band will stretch, causing changes in the Received Signal Strength Indicator (RSSI), which we then use to infer breathing patterns.

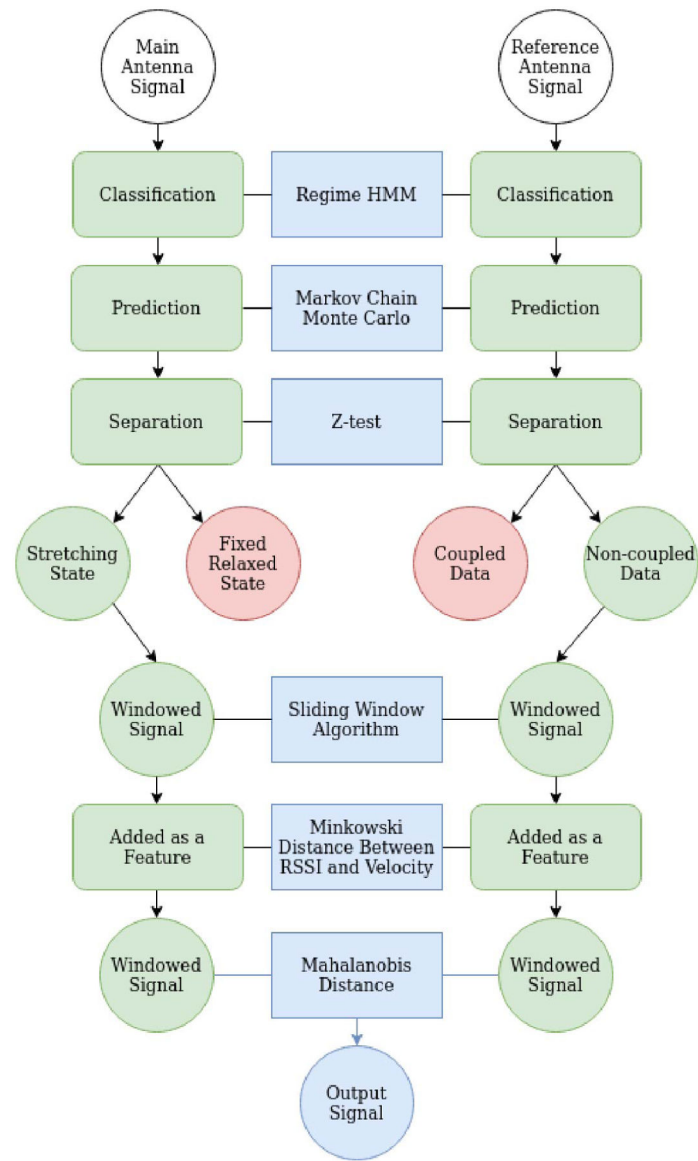


Figure 2:
Outline of each processing step of the algorithm.

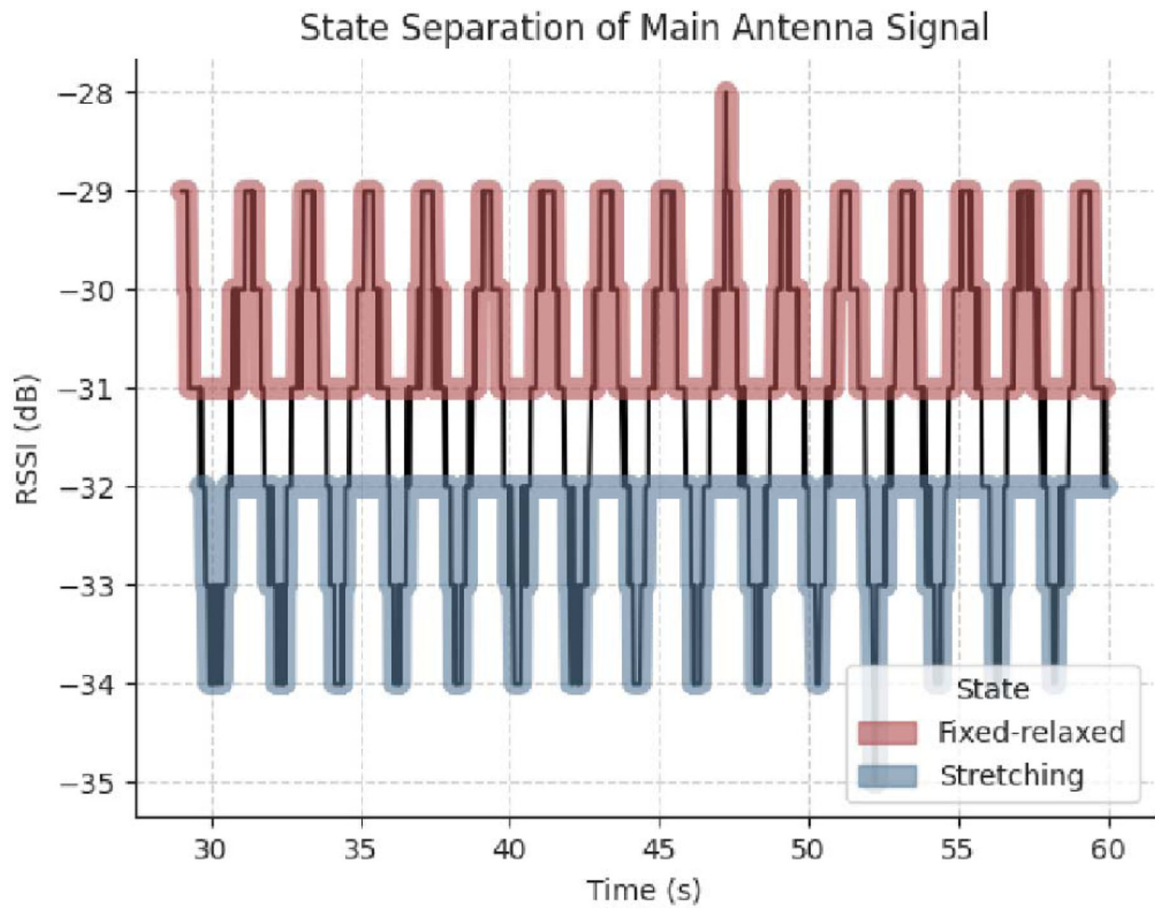


Figure 3:

A plot illustrating the separated states of the main antenna in comparison to its input signal. The highlighted segments of the input signal are those that correspond to one of the antenna's two states.

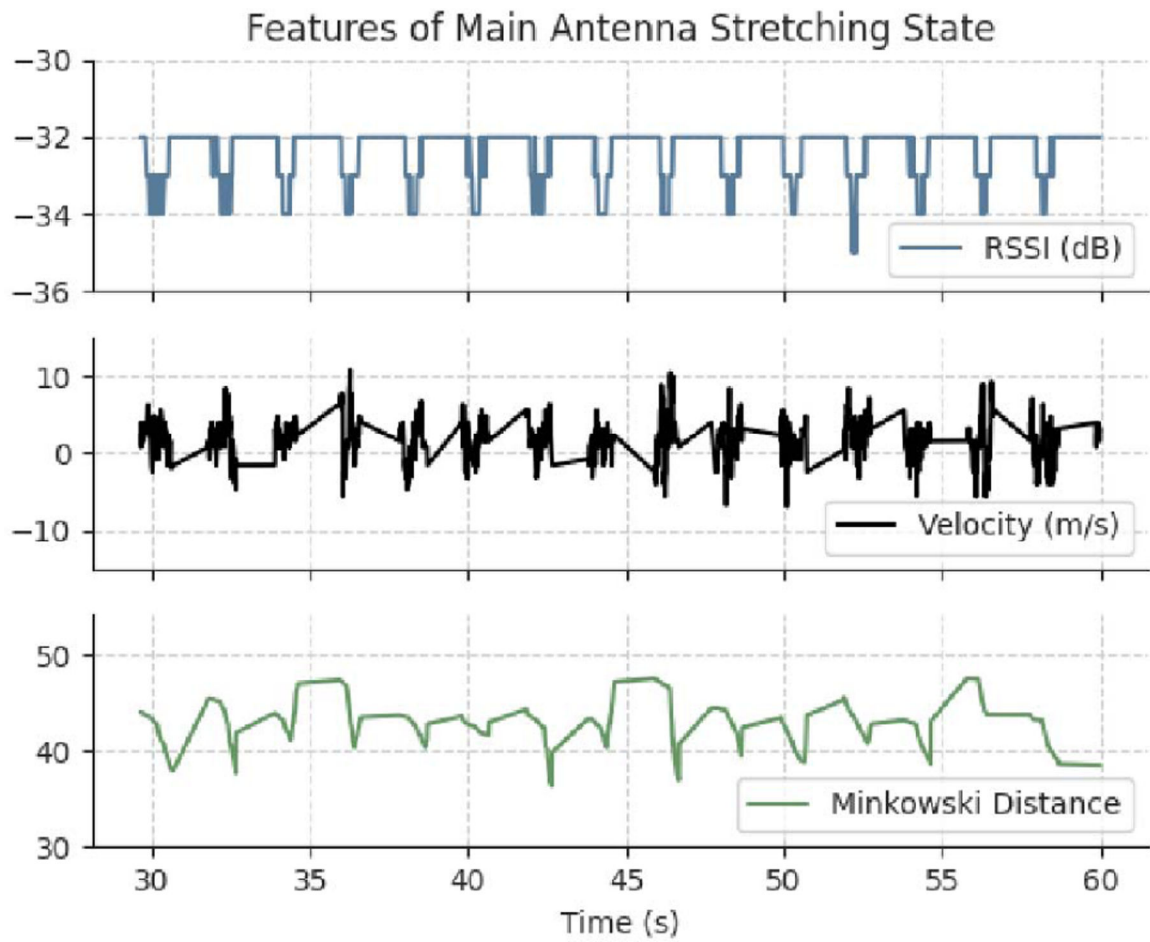


Figure 4:

A plot of the three features of the main antenna's signal used for the Mahalanobis distance:

i.) RSSI in *dB*, ii.) Velocity in *m/s*, iii.) Minkowski distance.

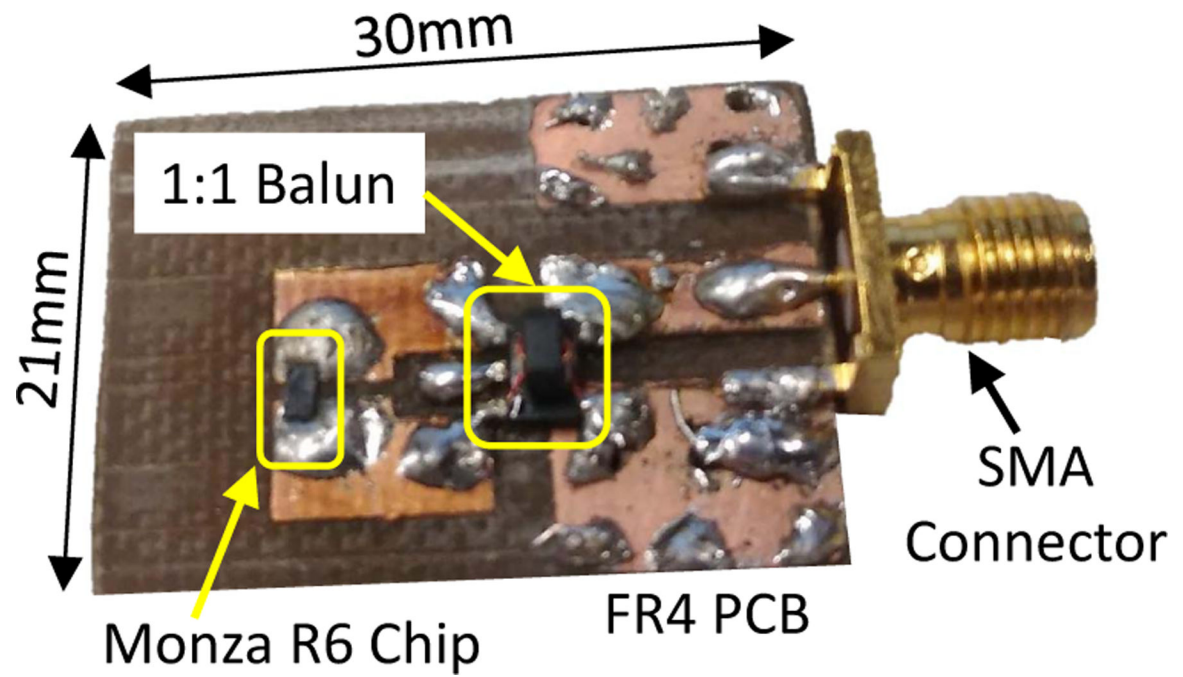


Figure 5:
Custom circuit board for RFID channel emulation experiment.

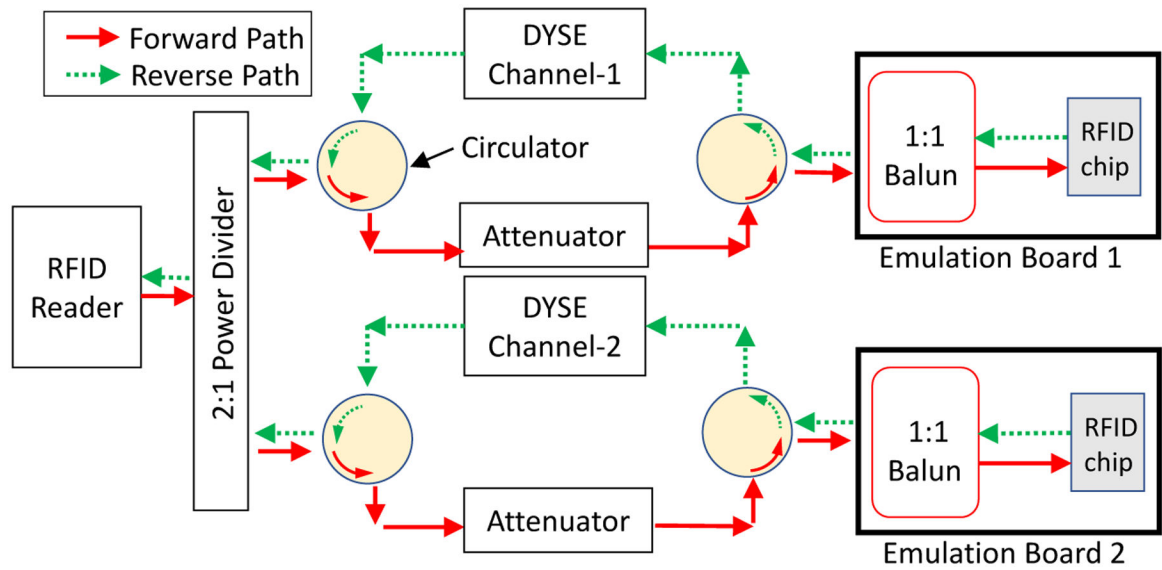


Figure 6:
Block diagram of the multiple channel emulation setup.

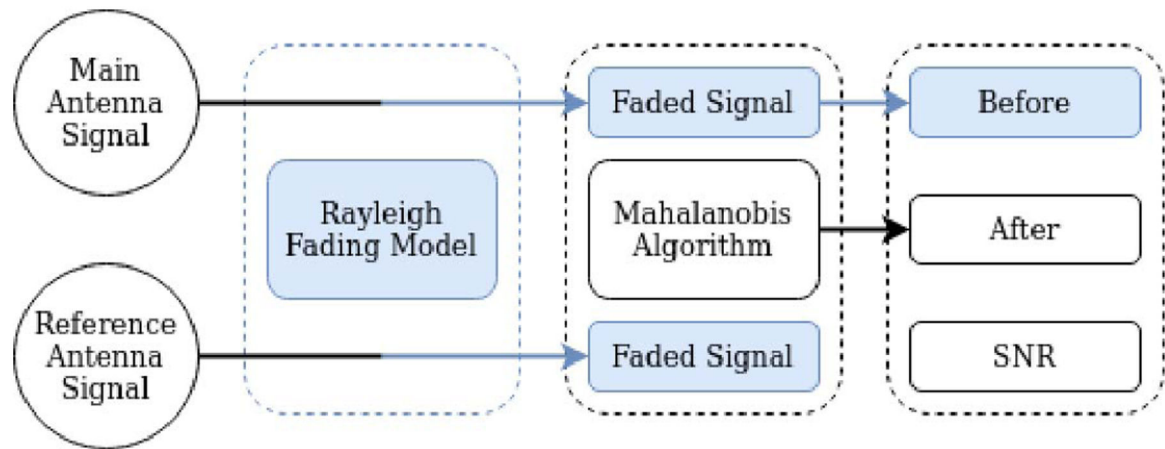
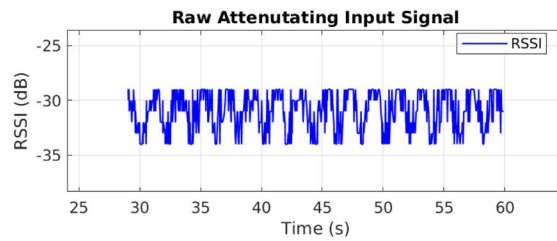
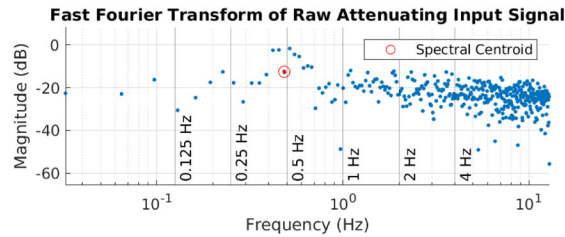


Figure 7:

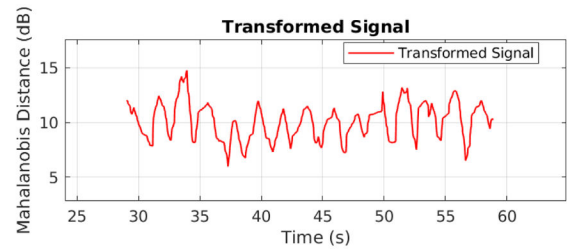
The experimental setup using emulated data. The faded signals are the input signals of Fig. 2. The main antenna and output signals of Fig. 2 are used in the SNR calculation.



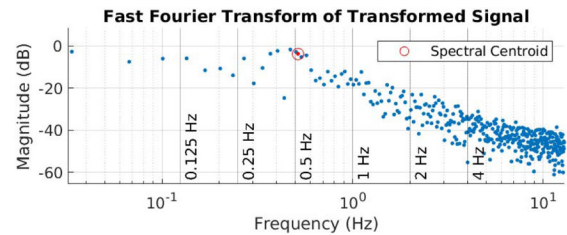
(a) Raw input signal of attenuating antenna.



(c) FFT of raw attenuating signal. The presence of high-frequency components can be seen above 1 Hz.



(b) Transformed signal.



(d) FFT of transformed signal. Unwanted high-frequency components above 1 Hz have been filtered out.

Figure 8:

The input signal, its transformation, and their respective FFTs from our emulated experimental setup with a breathing rate of 30 breaths per minute, a window size $n = 1$ second, a window slide $k = 0.25$ seconds, and a noise scale $C = 3$.

The results of each set of experiments using emulated data. Each row contains outputs averaged over 20 trials for each value used for noise scale C . Here, $P_{\text{signal,dB}}$ is the magnitude of the spectral centroid as outlined in Section IV-D, the magnitude of which is measured in decibels (dB).

Table I:

Average:	Raw Signal SNR	Raw Signal $P_{\text{signal,dB}}$	Transformed Signal SNR	Transformed Signal $P_{\text{signal,dB}}$	Increase in SNR
15 breaths per minute, 2 second sliding window.					
$C=1$	22.17 dB	-5.30 dB	46.75 dB	9.11 dB	24.58 dB
$C=2$	20.99 dB	-3.74 dB	39.30 dB	-1.28 dB	18.30 dB
$C=3$	20.20 dB	-2.94 dB	33.66 dB	-9.03 dB	13.46 dB
30 breaths per minute 1 second sliding window.					
$C=1$	16.57 dB	-10.71 dB	26.25 dB	-9.84 dB	9.67 dB
$C=2$	12.98 dB	-11.84 dB	30.88 dB	-8.33 dB	17.89 dB
$C=3$	9.80 dB	-13.68 dB	31.61 dB	-7.45 dB	21.81 dB